



Progressive activation of degradation processes in solid oxide fuel cell stacks: Part II: Spatial distribution of the degradation

Arata Nakajo^{a,*}, Fabian Mueller^b, Jacob Brouwer^b, Jan Van herle^a, Daniel Favrat^a

^a Laboratoire d'Energétique Industrielle (LENI), Institut de Génie Mécanique, Ecole Polytechnique Fédérale de Lausanne, 1015 Lausanne, Switzerland

^b National Fuel Cell Research Center, University of California, Irvine, CA, United States

H I G H L I G H T S

- Analysis of the combined effect of multiple degradation processes in SOFC stacks.
- Distribution and interactions between degradation phenomena in SOFC stacks.
- Simulation of the effects of stack design and operation on lifetime.
- Counter-flow lowers cathode Cr contamination, compared with co-flow.
- Components stacking practically affects the choice of optimal operating conditions.

A R T I C L E I N F O

Article history:

Received 1 March 2012

Received in revised form

19 May 2012

Accepted 21 May 2012

Available online 1 June 2012

Keywords:

Solid oxide fuel cell

Degradation

Chromium contamination

Creep

A B S T R A C T

Solid oxide fuel cell (SOFC) stack design must yield the highest performance, reliability and durability to achieve the lowest cost of electricity delivered to end-users. Existing modelling tools can cope with the first aim, but cannot yet provide sufficient quantitative guidance in the two others.

Repeating unit models, with as degradation processes the decrease in ionic conductivity of the electrolyte, metallic interconnect corrosion, anode nickel particles coarsening and cathode chromium contamination are used to investigate their distribution, evolution and interactions in a stack. The spatial distribution of the degradation is studied for the operating conditions optimised in Part I for the highest system electrical efficiency during long-term operation under constant system power output.

Current-voltage characterisations performed at different times underestimate the degradation. In the present conditions, the degradation of the cathode dominates. The lower and more uniform cathode overpotential in counter-flow configuration, combined with the beneficial effect of internal reforming on reducing the air-fuel ratio yields the highest lifetime, because it alleviates chromium contamination and interactions between the degradation processes. Increasing the operating temperature alleviates cathode chromium contamination. The beneficial decreases of the cathode overpotential exceed the detrimental higher release rate of chromium species from the metallic interconnect.

© 2012 Elsevier B.V. All rights reserved.

1. Introduction

The requirements that a solid oxide fuel cell (SOFC) stack must meet depend on the application foreseen by the end-user. Specifications are typically defined in terms of electrical efficiency, power density, thermal and load cycling capabilities and threshold costs for commercial viability. They have a strong impact on the stack design, since they govern the choice of technological solutions, such as the type of cell and sealing system.

SOFC technology does not yet meet the reliability and durability targets for large-scale commercialisation. Even though materials improvement plays the central role in the development process, system and stack design must integrate degradation analysis to achieve the lowest cost of electricity. The transient behaviour and compatibilities between the materials of the stack and the system must be adapted to fulfil utility grid support, fuel flexibility and lifetime specifications. The optimal operating conditions for the stack alone and after implementation in the system differ, because of parasitic power consumptions in the system, such as that due to the air blower. The achievement of the lowest stack pressure drop, while ensuring a uniform distribution of the gases over the whole power modularity of the stack, is crucial.

* Corresponding author. Tel.: +41 21 693 35 05.

E-mail addresses: arata.nakajo@epfl.ch, arata.nakajo@uconn.edu (A. Nakajo).

Different modelling tools must be combined to tackle all the aforementioned aspects that determine whether a stack and system design is economically viable or not. Studies based on a one-dimensional description along the gas channels of the single repeating units (SRU) are useful to identify trends. Their low computational demand is often compatible with optimisation. In a stack, a completely even distribution of the reactants to the electrochemically-active sites in each cell cannot be guaranteed, since stacking constrains the gas manifold. Even though the SRU design achieves an almost one-dimensional variation of cathode and anode gas composition, temperature, overpotential and current density, performance and degradation issues may arise from geometrical particularities. Thermo-electrochemical models usually focus on the zones where gases circulate. Yet, critical mechanical failures occur in sealing areas as well. An apparently simple temperature profile can generate a complex stress field. Therefore, dedicated analysis on temperature and gas flow distribution [1–4], transient behaviour [5–8], structural issues [9–13] and effects of stack component imperfections [14–16], are commonly performed on actual geometries. Such studies anticipate degradation by typically preventing the reoxidation of the anode and high local rates of heat generation to limit the temperature difference and/or local thermal gradients in the SRU.

Because durability is the main hurdle to overcome before the commercialisation of SOFC devices, model-based analyses of the degradation at the SRU scale, including a detailed geometry or not, are available from the literature. Most of them currently provide information specifically on electrode contamination [15] or delamination [16], for instance, but do not include time. Therefore, accelerating effects due to interactions between the phenomena, that cause a higher degradation rate during endurance test of stacks, compared with button cells, cannot be captured. Studies seeking to provide lifetime predictions remain sparse [17] and their relevance somewhat limited by the considerable variations in the dominating degradation phenomena, and further, by controversy on the mechanisms.

Degradation is, in broad terms, induced by localised physico-chemical alterations of the materials. Investigations at this scale are therefore the main means to extend the lifetime of SOFC. However, since degradation processes exhibit temperature, gas composition and overpotential or current density dependence [18–24], adequate operating conditions can alleviate their detrimental effects on the long-term stack performance. System layout and control strategy [5,6,25] may herein play a key role to improve the durability of SOFC devices. This is a practical approach that has received limited interest so far.

This modelling study investigates the effect of the operating conditions on the degradation of SOFC planar, intermediate-temperature stacks based on anode-supported cells under practical conditions. In Part I [26], optimisation has been carried out using a one-dimensional SRU model with degradation and system considerations in the view of the highest electrical efficiency at start-up and at long-term operation in constant system power output mode. This Part II focuses on a specific SRU design to study the evolution of the degradation patterns over the active area, and the detrimental interactions between the phenomena. A local one-dimensional electrochemical model that includes the decrease of ionic conductivity of 8YSZ, anode nickel particle growth, corrosion of the metallic interconnect (MIC), chromium contamination and formation of zirconates (LZO, SZO) in the composite lanthanum-strontium manganite and yttria-stabilised zirconia (LSM–YSZ) cathode, is implemented in two SRU models, with either a one or two-dimensional in-plane discretisation. The evolution of the area specific resistance (ASR), the distribution of the degradation and interplay between the different contributions, are investigated

during degradation simulations at varying constant system electrical power output, interrupted every 1500 h for current–voltage (IV) characterisation and comparison at a reference operating point. The contribution of stacking issues due to possible fuel feed limitation of an SRU in a stack, arising from the lack of reproducibility of the mechanical properties of the stack components, is assessed by computing the creep strain rate in the anode gas-diffusion layer (GDL) and adapting the anode gas flow accordingly.

2. Modelling approach

The frame of the present study is a 2.5 kWe SOFC stack design developed in the FP6 European FlameSOFC project for implementation in a combined heat and power unit. Fig. 1 depicts the SRU design. Unlike the original project, where fuel processing was based on thermal partial oxidation, steam-methane reforming is considered here, because of the higher achievable efficiencies. The thermo-electrochemical models are implemented in gProms, an equation-oriented process modelling tool [27].

2.1. One-dimensional electrochemical model

A one-dimensional electrochemical model that includes degradation processes is implemented in two SRU models. The detailed

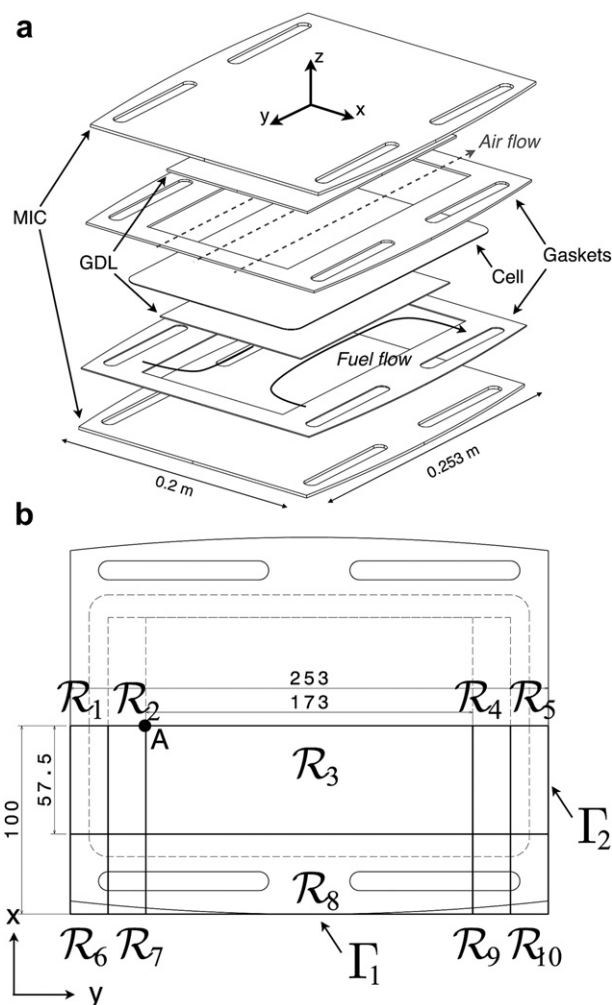


Fig. 1. (a) View of the FlameSOFC SRU design and (b) computation domains in the 2D SRU thermo-electrochemical model. \mathcal{R} : domains, Γ : boundaries.

description of the modelling approach of the electrochemical model was provided in Ref. [28], along with the calibration on experimental data from two different segmented-cell setups. The main features are recalled hereafter:

- Ohmic losses comprise the ionic resistivity of the electrolyte, corrected for constriction effects; the electronic resistivity of the MIC, its oxide layer and contact resistance; and a limited electronic conductivity of the electrolyte that induces a small leakage current.
- The LSM–YSZ cathode is described by a composite electrode model that solves the charge balance along with mass transport. The transfer current is computed following the sequence of elementary processes proposed by van Heuveln et al. [29], adapted for a low coverage of adsorbed oxygen species.
- On the anode side, the dusty-gas model is solved in one-dimension, through the thickness of the support, along with the equation of continuity. The steam-methane reforming rate is computed by the kinetic approach of Achenbach and Riesenke [30] and the water-gas shift reaction is assumed at equilibrium in the anode. Only hydrogen is electrochemically converted at the interface, following the set of elementary processes proposed by Zhu et al. [31].

This electrochemical model supports the implementation of a selection of degradation phenomena consisting in (i) the decrease in ionic conductivity of 8YSZ, (ii) MIC corrosion, (iii) anode nickel particle growth and, (iv) chromium contamination and (v) formation of zirconates in the LSM–YSZ cathode. The description of the modelling approach, the value of the parameters and the analysis of the behaviour under the typical range of conditions found in planar, intermediate-temperature SOFC stacks is provided in Ref. [32]. The main features of the degradation models are summarised in the following paragraphs.

2.1.1. Nickel particles coarsening

A classical percolation model predicts the reduction of the triple-phase boundary (TPB) due to the growth of nickel particles in the anode. The semi-empirical relation for the evolution of the nickel particle radius depends on temperature, steam and hydrogen partial pressure and the computed radius of the Ni particles tends to a maximum radius due to the mechanical constraint imposed by the YSZ network. In the model, the time to reach the plateau value spans from 1000 h to 10000 h [32] under the local conditions found in an intermediate temperature SOFC stack.

2.1.2. Decrease of the ionic conductivity of YSZ

An empirical model reproduces the experimental data on the decrease of the ionic conductivity of 8YSZ samples during ageing in air. The temperature-dependent plateau value is reached in the model after 500 h–2500 h [32]. The trend in the evolution after ageing during more than 5000 h is not included in the data. Errors may arise from extrapolation. This degradation process affects both the electrolyte and the 8YSZ phase in the LSM–YSZ cathode. Recovery of the ionic conductivity is not allowed.

2.1.3. MIC corrosion

The maximum SRU temperature in intermediate-temperature SOFC is limited, among others, by the oxidation resistance and high-temperature mechanical properties of the metallic components. This is not included in the present study, because a consistent set of data on the temperature dependence of the evolution of the area specific resistance (ASR) of coated MIC could not be found. The relation by Liu et al. [33] for the growth of the oxide scale under a $\text{Mn}_{1.5}\text{Co}_{1.5}\text{O}_4$ coating that is used in the present study is valid at 1073 K exclusively.

2.1.4. Chromium contamination of LSM–YSZ cathode

The modelling approach assumes the progressive blocking of the active sites by the electrochemical deposition of Cr_2O_3 from $\text{CrO}_2(\text{OH})_2(\text{g})$ released by the MIC and upstream system metallic components, described using a Butler–Volmer equation [32]. The release of volatile species is assumed governed by mass transport limitations, as suggested by Opila et al. [34]. The partial pressure of $\text{CrO}_2(\text{OH})_2(\text{g})$ over the oxide scale of the MIC is first assumed at equilibrium and computed from thermodynamic data for Cr_2O_3 [35,36]. For consistency, a small amount of steam is needed in the air. The value of 0.1% used here is typical for compressed air, commonly used in stack tests [20]. In the fully developed region of a laminar flow, the analogy between heat and mass transport, i.e. $Nu \cdot Pr^{n_t} = Sh \cdot Sc^{n_t}$ [37], simplifies the conservation equation of $\text{CrO}_2(\text{OH})_2$. The one-dimensional nature of the air flow in the FlameSOFC design yields:

$$u_{\text{air}} \frac{p_{\text{atm}}}{RT_g} \frac{\partial x_{\text{CrO}_2(\text{OH})_2}}{\partial y} = \mathfrak{R}_{\text{CrO}_2(\text{OH})_2}^{\text{vap}} + \mathfrak{R}_{\text{CrO}_2(\text{OH})_2}^{\text{dep}} \quad (1)$$

The vaporisation and deposition rates are:

$$\mathfrak{R}_{\text{CrO}_2(\text{OH})_2}^{\text{vap}} = -\frac{1}{h_{\text{air}}} \left[\frac{p_{\text{atm}}}{RT} \frac{Nu D_{\text{CrO}_2(\text{OH})_2}^e}{L} (x_{\text{CrO}_2(\text{OH})_2} - x_{\text{CrO}_2(\text{OH})_2}^{\text{eq}}) \right] \quad (2)$$

$$\mathfrak{R}_{\text{CrO}_2(\text{OH})_2}^{\text{dep}} = -\frac{1}{h_{\text{air}}} \frac{i_{o_{\text{D}_{\text{cath}}}} x_{\text{CrO}_2(\text{OH})_2}^{1/2} x_{\text{H}_2\text{O}}^{1/2}}{A_{\text{R}_{\text{area}}} F} \int_{z=0}^{z=h_{\text{cath}}} v_{\text{cath}}(z) A_{\text{TPB}}(z) 2 \sin h \left(\frac{1 F \eta_{\text{cath}}(z)}{2 RT_s} \right) dz \quad (3)$$

As a first approximation, $D_{\text{CrO}_2(\text{OH})_2}^e = 2.25 \cdot 10^{-5} \text{m}^2 \text{s}^{-1}$ [15].

2.1.5. Zirconate formation in the LSM–YSZ cathode and anode reoxidation

Indicators are used for the risk of reoxidation of the anode [17] and formation of undesirable zirconate phases (LZO, SZO) in the LSM–YSZ cathode. For the latter, the thermodynamic data on the critical oxygen partial pressure from Liu et al. [21] is interpolated and compared with the local one, computed from the local overpotential and oxygen gas phase concentration.

This approach significantly simplifies the real situation in an SOFC stack:

- In ferritic alloys for SOFC application, a $(\text{Mn,Cr})_3\text{O}_4$ spinel develops on top of the oxide scale [38]. It alleviates the release of chromium species, due to the thermodynamic equilibrium, as shown by computations for MnCr_2O_4 in humid air [39]. The situation is further complicated in a coated MIC. The use of thermodynamic data for the equilibrium partial pressure of $\text{CrO}_2(\text{OH})_2$ over Cr_2O_3 therefore yields conservative lifetime predictions, even though the scatter in the thermodynamic data induces imprecision in the range of one order of magnitude [15,34,39]. Other volatile species than $\text{CrO}_2(\text{OH})_2$ may be also involved in reality [40–43]
- Resistance against mass transport of $\text{CrO}_2(\text{OH})_2$ from the air channel to the active sites where it is electrochemically deposited, is neglected. This assumption is conservative, but prevents the use of the model for reliable guidance in the choice of the cathode thickness or microstructure or current collector materials that may act as a contamination-protecting layer.

Table 1
Thickness of the main SRU components.

	Electrolyte	Cathode	Anode	GDL _a	GDL _c	MIC
Material	8YSZ	LSM–YSZ	Ni–8YSZ	Ni	LSM	Crofer22APU ^a
h (m)	7e-6	60e-6	540e-6	1e-3	2e-3	2e-3

^a Commercial denomination of ferritic alloy [59].

- Depending on the humidity, other phenomena, not necessarily related to chromium contamination, may predominantly cause the degradation of the LSM–YSZ cathode [44]. Chromium contamination and air humidity affect LSCF and lanthanum strontium ferrite cathodes as well, but the degradation mechanisms differ [44–46]. This restricts the use of the chromium contamination modelling approach developed here to LSM–YSZ.

The present modelling approach partially captures the complexity of SOFC degradation, because the underlying physics is highly dependent on the materials and conditions and the understanding is in progress. It however reproduces the correct trends, without any specific adjustment, as shown in Ref. [32], but cannot comply with all the observations from post-mortem analyses [22,23,47] under any tested conditions. For such an achievement, the number of implemented degradation mechanisms and the level of refinement in their description must be increased, which requires in future a more intricate interrelationship between experiments and modelling.

2.2. SRU thermo-electrochemical models

The two thermo-electrochemical SRU models are based on similar assumption [12,28] but differ in term of in-plane discretisation. In the first one, the SRU geometry is discretised in one-dimension along the flow path and described in Ref. [28]. In the second one, the in-plane discretisation is two-dimensional and the geometry is divided into 10 sub-domains (see Fig. 1), because of the limited flexibility for geometry discretisation in gPROMS. These comprise the electrochemically active area \mathcal{R}_3 , sealing areas \mathcal{R}_6 to \mathcal{R}_{10} , fuel (\mathcal{R}_2 and \mathcal{R}_4) and air (\mathcal{R}_1 and \mathcal{R}_5) introduction and exhaust

zones. The fuel manifold is not meshed and restricted to boundaries $\Gamma_{\mathcal{R}_2\mathcal{R}_7}$ and $\Gamma_{\mathcal{R}_4\mathcal{R}_9}$. The field equations are solved in the in-plane directions and coupled to the local one-dimensional electrochemical model. The properties of the solid structure are averaged. In both SRU models, the boundary conditions are imposed to simulate an SRU in a large stack. The Appendix provide a brief description of the two-dimensional SRU model, whereas that of the one-dimensional model is available in Ref. [28].

In a first approximation, the main auxiliary losses of a typical system for CHP application, comprising as main components an evaporator, a reformer, a combustor and a network of heat exchangers in addition to the fuel cell can be simplified to the parasitic power consumption of the air blower and inverter [6]. Their simplified modelling is identical in the two SRU models. The power consumption of the air blower per SRU in the stack is computed using isentropic relations and an isentropic efficiency of 0.8. The stack air side pressure drop is computed using an empirical relation for the permeability of metallic foams [48]. That of the heat exchanger network is coarsely approximated to be twice that of the stack. The inverter efficiency of 93% is assumed constant.

A simple implementation of creep in the model provides an assessment of the impact of uneven fuel supply among SRUs in a stack, due to the disparities in the mechanical properties of their anode GDL (see Appendix).

3. Investigated cases

3.1. Optimisation procedure

Optimisation has been performed in Part I to identify the operating parameters that predominantly affect the lifetime, under the present model assumptions. The same sequential procedure as that used by Larrain et al. [49] has been used. It consists in performing optimisation on one objective, the other being subjected to a constraint that is sequentially adapted to cover the desired range of variation. The conflicting objectives were the system specific electrical power, from 0.18 to 0.35 W cm⁻², and the system efficiency. The time horizon in the dynamic optimisation influences which degradation phenomena are predominantly alleviated. A

Table 2
Typical conditions in the two-dimensional model during operation, IV characterisation procedure and comparison at a reference point procedure. The system specific power is 0.29 W cm⁻² and the maximum SRU solids temperature is 1125 K. PR: methane conversion fraction in the reformer.

Flow configuration	COU			CO			CO		
PR	0.25			0.99			0.99		
Time (h)	0	3000	4500	0	3000	4500	0	3000	4500
Constant system specific power									
U (V)	0.73	0.67	0.64	0.73	0.67	0.65	0.71	0.65	0.62
j (A cm ⁻²)	0.44	0.48	0.50	0.45	0.49	0.51	0.45	0.50	0.53
FU ^a	0.84	0.84	0.84	0.84	0.84	0.84	0.84	0.84	0.84
T_{air} ^a	975	975	975	987	987	987	985	985	985
Fuel flow [nplm cm ⁻²]	3.19	3.46	3.63	4.62	5.06	5.28	4.60	5.09	5.39
Air ratio	6.5	7.5	7.91	9.9	10.7	11.1	9.3	10.1	10.6
IV (FU = 0.9, j = 0.42 A cm ⁻²)									
U (V)	0.72	0.70	0.69	0.72	0.69	0.68	0.72	0.68	0.67
T_{air}	973	973	973	973	973	973	973	973	973
Fuel flow (nmplm cm ⁻²)	2.89	2.89	2.89	4.11	4.11	4.11	4.11	4.11	4.11
Air ratio	6.27	6.27	6.27	8.90	8.90	8.90	7.90	7.90	7.90
Reference point									
U (V)	0.73	0.69	0.68	0.72	0.68	0.67	0.73	0.69	0.67
j (A cm ⁻²)	0.44	0.44	0.44	0.46	0.46	0.46	0.44	0.44	0.44
FU	0.85	0.85	0.85	0.84	0.84	0.84	0.84	0.84	0.84
T_{air}	975	975	975	987	987	987	985	985	985
Fuel flow (nmplm cm ⁻²)	3.18	3.18	3.18	4.72	4.72	4.72	4.60	4.60	4.60
Air ratio	6.5	7.2	7.6	9.8	10.5	10.7	8.6	9.2	9.4

^a Constant during operation.

lifetime criterion that can be used over the full investigated range is not straightforward to select and to implement in an optimisation problem. A fixed value of 2000 h has been used to limit numerical failures, yet to ensure that the long-term degradation characteristics are captured.

Because of the incomplete understanding of SOFC degradation and of computation time reasons, an optimisation problem can currently not include all the phenomena that may limit the lifetime of SOFC systems. Mechanical aspects are relevant as well, but are not included in the present thermo-electrochemical analysis. Therefore, several optimisations were performed for discrete values of the decision variables that are believed to have the most significant effect on the temperature profile to support further analyses [50,51]:

- The maximum allowable SRU temperature (1100 K, 1125 K, 1150 K).
- The methane conversion fractions in the reformer (25%, 50%, 99%).

These ranges are typical for intermediate-temperature, anode-supported SOFC stacks. Mixed integer non-linear programming was not used. Hence, optimisation was performed separately for the co and counter-flow configurations. The continuous decision variables that were optimised are:

- The fuel utilisation, between 0.6 and 0.95.
- The air inlet temperature, between 600 and 1080 K.

3.2. Simulated procedures

The analysis of the distribution of the degradation is performed in this Part II for the operating conditions optimised in Part I for three values of the system specific power, 0.21, 0.25 or 0.29 W cm^{-2} . These conditions are selected for degradation analysis, under practical operating conditions, not for the comparison between the one- and two-dimensional in-plane discretisation. Differences between the true and idealised one-dimensional geometry may slightly modify the optimal values of the decision variables for the two in-plane discretisations of the SRU. A main reason is the addition of the sealing areas R_6 to R_{10} in the two-dimensional description that lowers the required air ratio to maintain a fixed maximum cell temperature, due to thermal conduction in these zones, compared with the one-dimensional description. Another difference, with an opposite effect, is the localisation of zones of high temperature due to anode gas distribution and geometry. The parasitic air blower power consumption accordingly varies but does not change the trends. Table 1 lists the thicknesses of the key components.

The evolution of the ASR is monitored during ageing at a constant specific system power simulated by the one-dimensional model, interrupted every 1500 h for characterisation. Two different procedures are compared to assess the severity and distribution of the degradation:

- *Procedure I.* IV characterisation up to a fuel utilisation of 0.9 is simulated under constant gas fluxes that initially yield a maximum temperature of 1125 K at 0.4 A cm^{-2} and a fuel utilisation of 0.85, with gas inlet temperatures of 973 K. The gas fluxes have to be adapted depending on the methane conversion fraction in the reformer to yield comparable conditions. Degradation phenomena are disabled during IV characterisations.
- *Procedure II.* The SRU is set at a reference operating point. The maximum allowable temperature is 1125 K. The fuel utilisation, air inlet temperature are those optimised in Part I for the

highest electrical efficiency at long-term, for a constant system specific power of 0.29 W cm^{-2} and a maximum cell temperature of 1125 K. The current density, rather than the system or stack specific power, is fixed for characterisation at the reference point. Its value is that determined with the stack performance at start-up, under the aforementioned optimised operating conditions. Different reference points are therefore selected for the co- and counter-flow configuration and for methane conversion fraction in the reformer.

The aim of Procedure II is to limit the evolution of the temperature profile during IV characterisations with constant gas flow (Procedure I), because of the degradation. The evolution of the distribution of the degradation over the active area is performed with the aforementioned procedure applied to the 2D model, for a specific system power of 0.29 W cm^{-2} and methane conversion fraction in the reformer of 0.25 (co-flow) and 0.99 (counter-flow). Table 2 summarises the operating conditions. Investigation on the

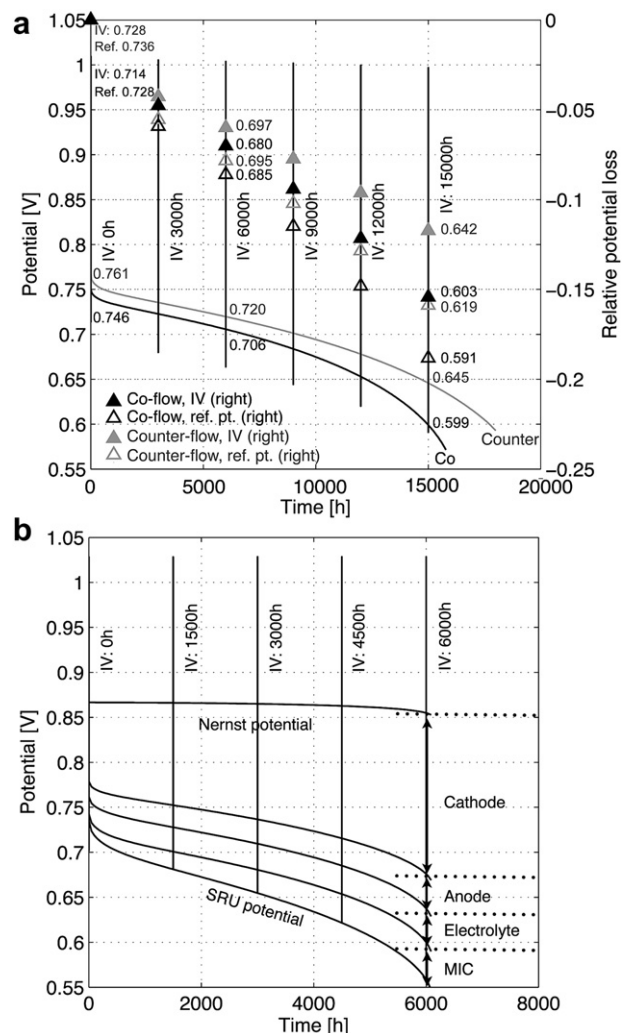


Fig. 2. Test sequence. (a) Lines: evolution of the potential during operation at a constant specific system power of 0.21 W cm^{-2} , a maximum SRU temperature of 1125 K and methane conversion percentage in the reformer of 25%. Markers: relative drop in potential measured during IV characterisations and by comparison with a reference point every 1500 h. Indicated values refer to the actual potential. (b) Contributions to the total overpotential in the counter-flow configuration, at a constant specific system power of 0.29 W cm^{-2} , a maximum SRU temperature of 1125 K and methane conversion in the reformer of 25%. The Nernst potential is computed at the anode/electrolyte interface.

risks of formation of zirconates in the LSM–YSZ cathode is performed for constant SRU specific power output of 0.32 W cm^{-2} , a maximum SRU temperature of 1125 K and similar inlet conditions than in Table 2.

The simulation of a progressive fuel undersupply of an SRU in a stack, due to an increased compression creep strain rate resulting from disparities in the mechanical properties, uses the one-dimensional SRU model and the conditions optimised in Part I for the highest system efficiency at start-up. The fuel flow is adapted from the creep deformation (see Appendix), whereas the current density, instead of system specific power, is kept constant.

4. Results and discussion

4.1. Averaged degradation indicators

This section provides the evolution of averaged indicators, along with insights on the reasons that are further completed in Section 4.3 and Section 4.4. The detailed instrumentation of an SOFC stack is difficult to achieve, which hinders the complete control and/or measurement of the field quantities during operation, IV and electrochemical impedance spectroscopy characterisations. Therefore, the choice of a stack test procedure is not trivial. IV characterisations are commonly performed at different operating times under fixed gas inlet conditions [22,52], even though they do not enforce the identical distribution of controllable quantities such as temperature, as the degradation proceeds.

Fig. 2 depicts the evolution of the simulated SRU potential and its relative loss during the simulated test sequence described in Section

3. The initial decay of the potential during operation is followed by a linear regime and final acceleration. In a first approximation, the first feature is caused by the degradation of the ionic conductivity of the electrolyte and reduction of TPB due to anode nickel particle coarsening. Both reach their plateau values in most of the active area, within 2000–3000 h (see Section 4.3). The accelerated degradation regime arises from the need to ever increase the current density to deliver a constant system electrical power output, because cathode chromium contamination proceeds and air blower losses increase to maintain the maximum SRU temperature within limits. In the conditions treated here, the cathode polarisation losses dominate. The contributions of the anode, MIC and electrolyte are much smaller and of comparable magnitude.

The simulated degradation pattern shown in Fig. 2 is in line with endurance tests of short stacks with anode-supported cells based on LSM–YSZ cathode [22,32]. Experimental measurements do, however, not always exhibit the initial decay because of overlapping activation processes that are not implemented in the model.

Fig. 3 depicts the IV characteristics simulated every 1500 h. This test procedure underestimates the relative potential loss due to operation at constant system specific power, compared with setting at a reference point, as observed in Fig. 2(a), because for fixed gas inlet conditions, the increase of the temperature indicated in Fig. 3(a),(c) masks part of the loss due to the degradation.

Fig. 3 shows that the degradation processes do not alter the overall pattern of either the IV or ASR curves. The contribution of the cathode exhibits the highest degradation, which evolves in an accelerated manner. The contribution of the ohmic losses in the

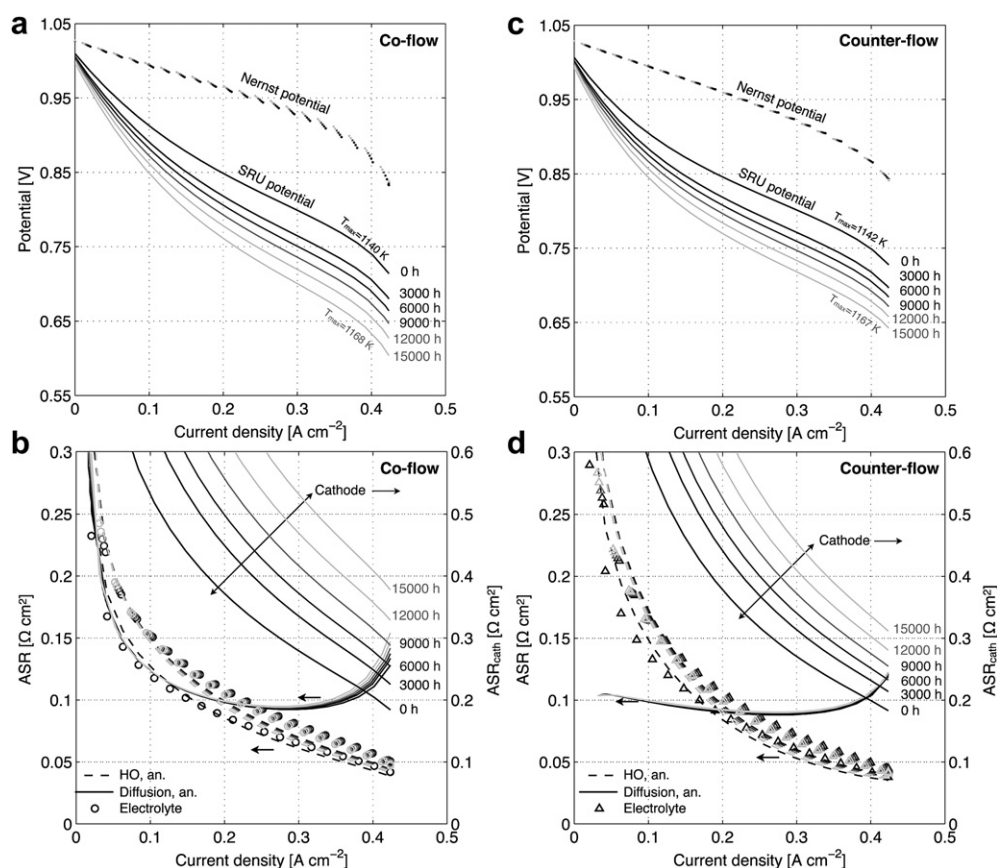


Fig. 3. IV characteristics recorded every 1500 h during operation at a constant specific system power of 0.21 W cm^{-2} and maximum SRU temperature of 1125 K (a) co-flow ($\text{PR} = 0.99$) and (c) counter-flow ($\text{PR} = 0.25$) configuration. Evolution of the contribution of the electrolyte, anode and cathode to the total ASR (b and d). The scale of the right axis for the cathode contribution is twice that of the left axis. HO: hydrogen oxidation.

electrolyte and the hydrogen oxidation on the anode side strongly increase at the beginning, and then stabilise because the variables governing their degradation in the model are close to their plateau value. The increase of the temperature throughout the characterisation times induces then a slight decrease of their value. The significant apparent dependence of the ohmic losses in the electrolyte on the current density arises from the evolution of the temperature profile throughout the IV characterisation. Even though the effect of any degradation phenomena on the anode porosity and tortuosity, such as nickel particle coarsening, is not implemented, the diffusion losses on the anode side detrimentally evolve in the co-flow configuration, but not in counter-flow. This is caused by the trade-off between temperature and anode gas composition, governing the location of the zone of highest local current density in co-flow (see Section 4.3). The degradation on the cathode side, which is the highest at the air inlet of the active area, limits the shift of maximum current density towards this zone, leaving high fuel utilisation and therefore anode diffusion losses towards the outlet. Counter-flow configuration is less prone to such detrimental redistribution of the current density, because high temperature and hydrogen-rich anode gas are available at the air outlet of the active area.

The investigation of the influence of the operating conditions on the degradation and the interaction at the SRU scale between the degradation processes is based on the evolution of the ASR at the reference point to reduce the temperature effects that affect IV characterisation. Fig. 4 depicts the effect of maximum SRU temperature and specific system power on the relative increase of the ASR of the electrolyte, hydrogen oxidation on the anode side and oxygen reduction on the cathode side. The methane conversion

fraction in the reformer that yields the highest lifetime is depicted, i.e. 0.25 and 0.99 in counter and co-flow, respectively. The chromium contamination of the cathode produces similar patterns in both flow configurations (Fig. 4(a) and (b)). The initial steep increase arises from the degradation of the 8YSZ ionic conducting phase in the composite cathode. The ASR further increases in an accelerating manner as Cr_2O_3 deposits block the active sites. Because of the benefit of decreasing the overpotential, the severity of the cathode degradation scales with power density and inversely with maximum SRU temperature and is lower in counter-flow.

The evolution of the ASR of the electrolyte and hydrogen oxidation on the anode side contrasts with that of the cathode. In the model, they are indirectly related to overpotential or current density, through temperature and gas composition, which results in a weak dependence on the system specific power (Fig. 4(c) and (d)). Both increase first steeply, reflecting the quick evolution of the variables controlling their degradation. Their increase after the first characterisation (1500 h) in the co-flow configuration is the result of detrimental interactions between the degradation processes at the SRU scale, as explained hereafter.

The nickel particle growth rate in the zone of high current density is lower in co-flow than counter-flow, owing to the lower temperature. The shift of this zone in the air flow direction, because of the degradation of the cathode, induces an increase of the polarisation losses for the hydrogen oxidation reaction, due to the apparent reaction orders of 1/4 on the hydrogen and steam molar partial pressures in the model [28]. The modelling of the degradation of the electrolyte comprises a temperature-dependent variable that reaches its plateau value after 2000 h in most of the active area in both co- and counter-flow configuration [32]. The

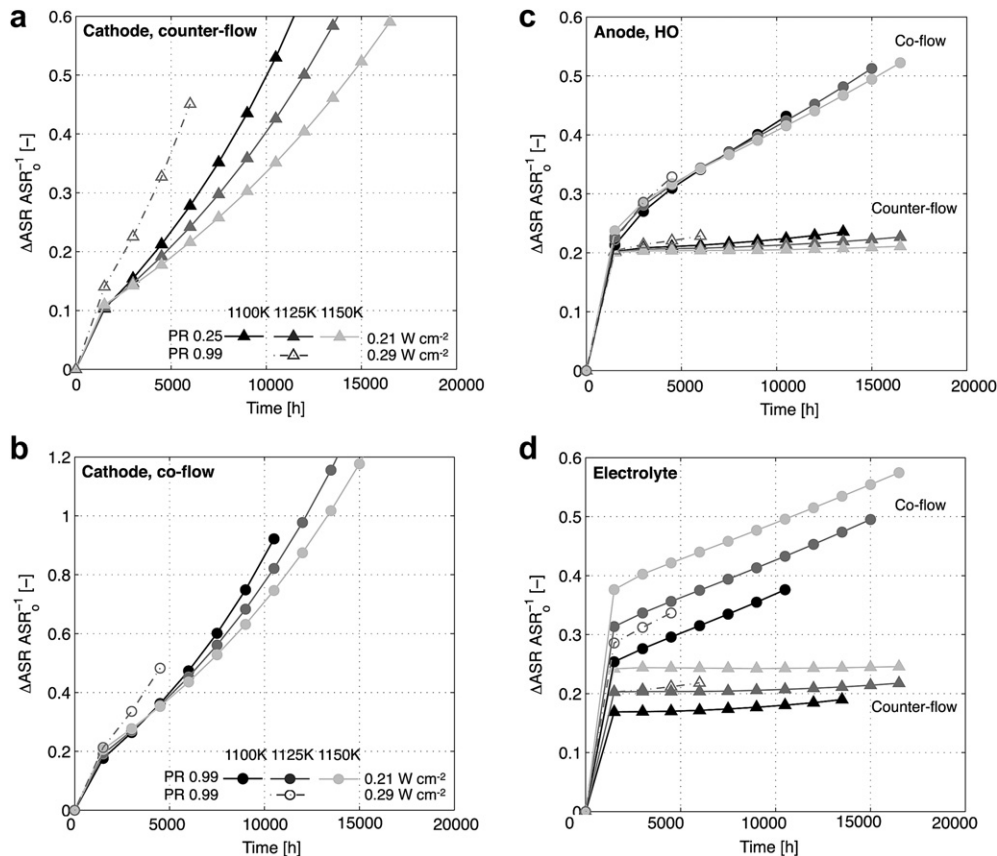


Fig. 4. Evolution recorded every 1500 h of the relative ASR of (a and b) the cathode, (c) H_2 oxidation and (d) electrolyte at the reference point, during operation at a different constant specific system power, flow configurations and maximum SRU temperatures. Note the scale doubling of the y-axis between (a) and (b).

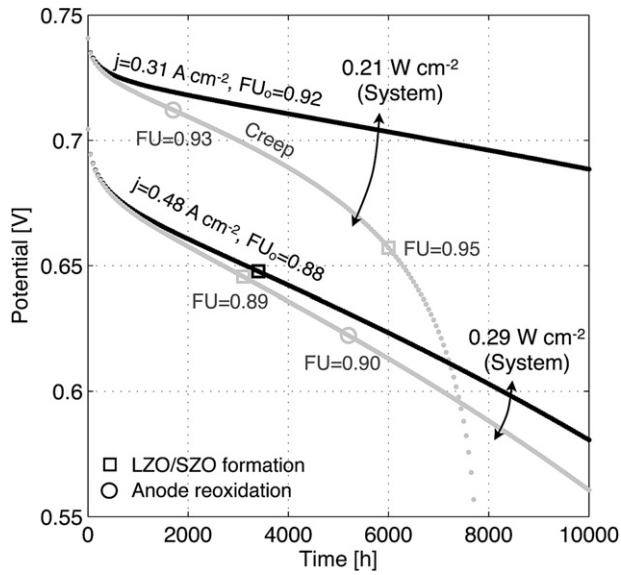


Fig. 5. Effect of creep in the anode GDL on the potential degradation during operation at a constant current density, corresponding to initial specific system power of 0.21 W cm^{-2} and 0.29 W cm^{-2} . Counter-flow configuration, 25% of pre-reformed methane and maximum allowable temperature of 1125 K. Empty markers indicate the occurrence of anode reoxidation and possible formation of LZO/SZO. Conditions for the highest system electrical efficiency at start-up (Part I).

variable yields more severe degradation at higher temperature. The subsequent increase of the electrolyte contribution to the SRU ASR in co-flow arises from a decrease of the average temperature over the active area due to the higher air ratio and displacement of the zone of higher current density away from the fuel inlet. This decrease in temperature in turn constrains the temperature-dependent final value of the degradation of the electrolyte. The counter-flow configuration is less prone to detrimental interactions between the degradation processes.

4.2. Stacking issues

Operation at a low specific power to extend the lifetime (Part I [26]) requires to stack more elements to achieve the targeted system power. The benefits of such an approach must be balanced by the increase of the risks of cell cracking, due to the larger volume of brittle ceramic material subjected to thermal stress, and gas distribution issues among the stacked SRU. In SOFC stacks, adequate reproducibility of the mechanical properties of the component materials and dimensional tolerances are difficult to achieve. It is for instance challenging to guarantee homogeneous conditions during the last manufacturing steps of a SOFC stack, such as the anode reduction or the sealing procedure, during which the mechanical properties of the anode and glass-ceramic sealing are modified.

Fig. 5 illustrates how mechanical aspects can contribute to the observed degradation of the electrochemical performance of a stack, by showing the effect of the reproducibility of the

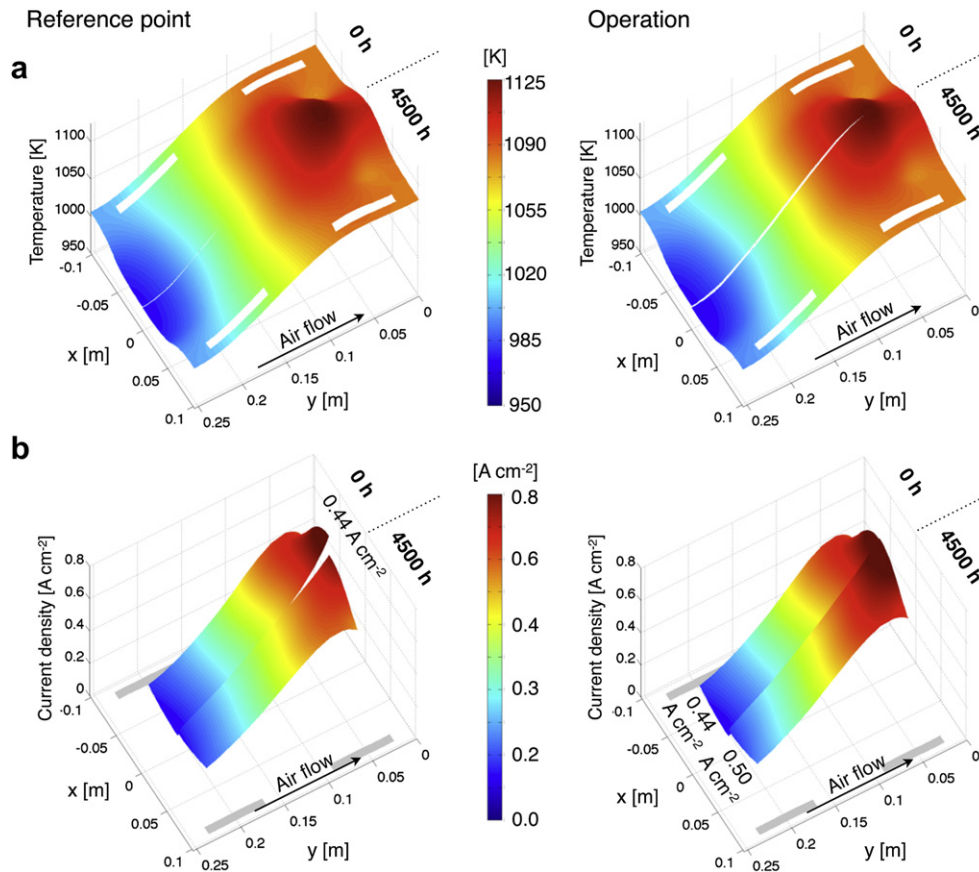


Fig. 6. Evolution of (a) the temperature profile and (b) current density observed after operation, following the test sequence depicted in Figure 2, at a constant system power of 0.29 W cm^{-2} . Left series: profiles at the reference point, right series: profiles during operation. Only half of the profiles are displayed. One side is the initial one ($t = 0 \text{ h}$), the other after ageing ($t = 4500 \text{ h}$). Counter-flow configuration, methane conversion of 25% in the reformer, maximum SRU temperature of 1125 K. The position of the fuel manifold is indicative.

mechanical properties of the anode GDL. This layer is for instance often based on a metallic foam, which exhibits a complex behaviour [53,54]. Here, a comparatively higher creep strain rate in an SRU embedded in a stack causes a progressive decrease of the fuel fed in this particular SRU. As the total current drawn from the stack remains unchanged, the fuel utilisation increases in an uncontrolled and unapparent manner.

Higher fuel utilisations can be typically achieved at lower system specific power, with a beneficial effect on the electrical efficiency. Fig. 5 suggests that structural issues may seriously hinder this advantage, due to an increased sensitivity on the creep behaviour of the anode GDL. The reoxidation of the anode and the formation of LZO/SZO occur earlier, because the redistribution of the current density affects the cathode degradation as well. In comparison, operation at a higher system specific power is less affected. Therefore, control strategy must be integrated with geometry design and manufacturing procedures to control the distribution of the contact pressure among adjacent materials and determine the safety margins for operation.

4.3. Effect of degradation on the distribution of the temperature, current density and overpotentials

Fig. 6 and Fig. 7 compare the temperature and current density distribution in the FlameSOFC SRU design at the initial time and after prolonged use. In counter-flow (Fig. 6), the localised zone of higher temperature at the air outlet of the active area (\mathcal{R}_3 in Fig. 1) results from the lateral fuel feeding along which the endothermic steam-methane reforming reaction proceeds and heat transfer

through thermal conduction in the sealing areas \mathcal{R}_6 to \mathcal{R}_{10} . It increases the magnitude of the maximum current density. As will be shown later, it has a limited effect on the cathode overpotential, and consequently the lifetime, but can result in detrimental stresses in the anode support [12,50,51] and loss of contact pressure on the compressive gaskets [13]. The current density flattens because chromium contamination principally affects the fuel inlet of the active area (see further Section 4.4). In operation, this is masked by the increase of the average current density to keep the system power constant. The effect of the degradation on the temperature profile is limited, owing to the fixed air inlet temperature and maximum SRU temperature. The slight increase of the temperature difference due to that of the air ratio, to maintain the maximum SRU solids temperature, is more visible during operation.

Fig. 7 shows the trade-off between temperature and lean fuel mixture that governs the location of the highest current density in the co-flow configuration. The zone of localised high temperature is less pronounced than in Fig. 6, owing to the complete methane conversion in the reformer and flow configuration. Heat transfer through thermal conduction in the sealing areas \mathcal{R}_6 to \mathcal{R}_{10} , slightly higher H_2 molar fraction, and the air cooling effect induce slightly higher current density at the junction between the gasket and the GDL (\mathcal{R}_3 and \mathcal{R}_8). As the degradation proceeds, the location of the highest current density is shifted towards higher temperature. This trend is amplified by the increase of the current density during operation at constant specific system power.

In the model, the overpotential is the dominant driving force for the chromium contamination of the cathode [26,32]. Fig. 8 depicts

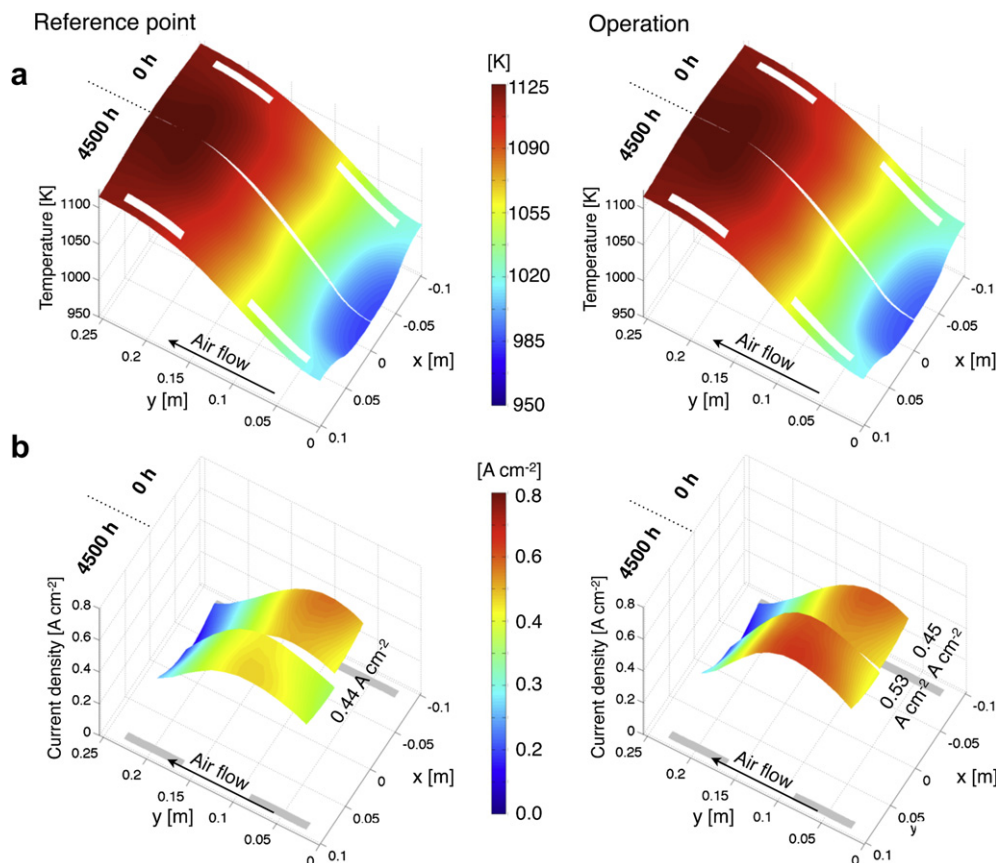


Fig. 7. Evolution of (a) the temperature profile and (b) current density observed after operation, following the test sequence depicted in Figure 2, at a constant system power of 0.29 W cm^{-2} . Left series: profiles at the reference point, right series: profiles during operation. Only half of the profiles are displayed. One side is the initial one, the other after ageing. Co-flow configuration, methane conversion percentage of 99% in the reformer, maximum SRU temperature of 1125 K. The position of the fuel manifold is indicative.

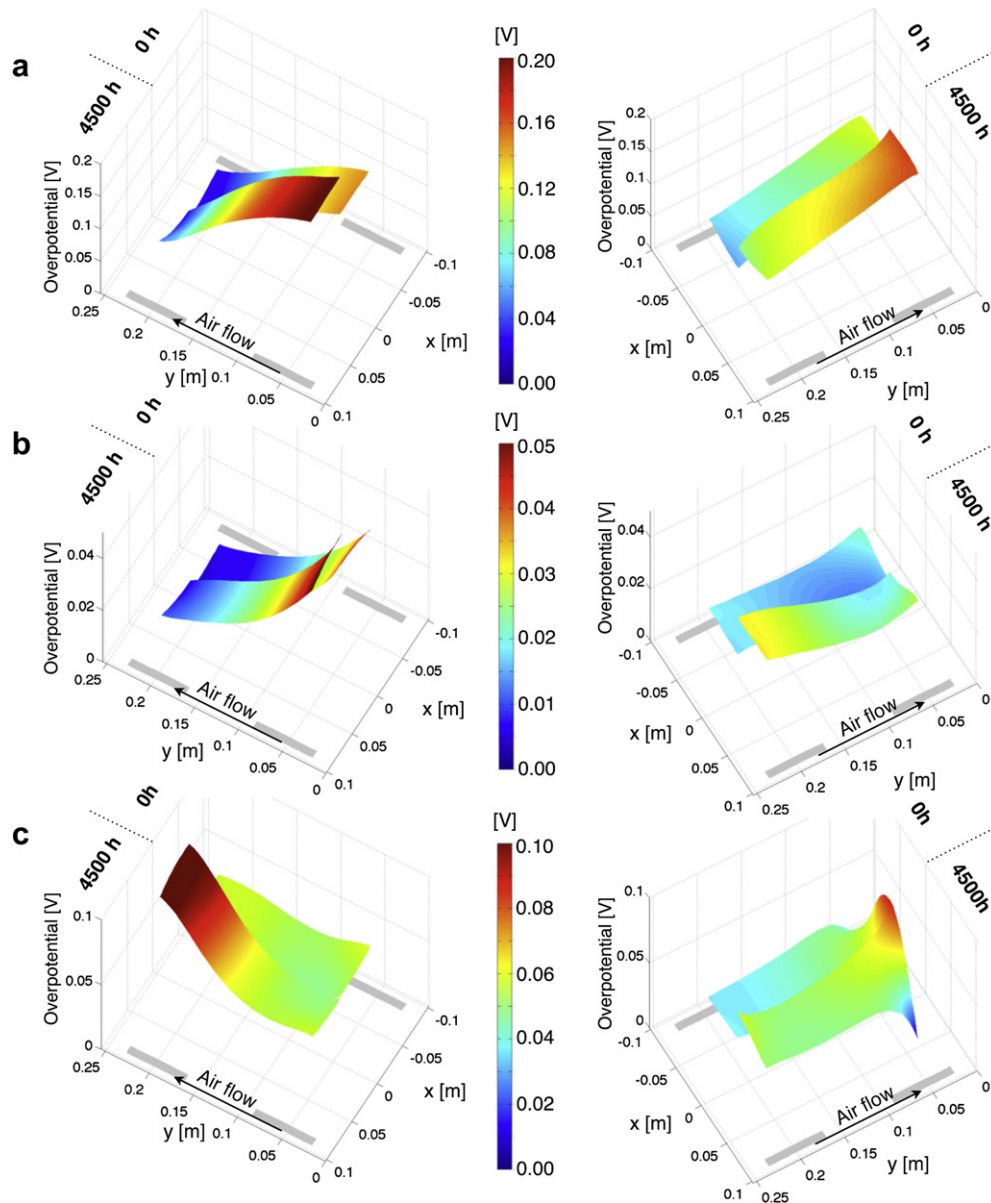


Fig. 8. Evolution of the overpotential profiles over R_3 due to (a) the oxygen reduction reaction, (b) hydrogen oxidation reaction and (c) diffusion on the anode side observed at the initial time and after 4500 h of operation at a constant system power of 0.29 W cm^{-2} . Left series: co-flow, methane conversion percentage of 99% in the reformer. Right series: counter-flow, methane conversion percentage of 25% in the reformer. Only half of the profiles are displayed, one side being the initial one, the other after ageing. The maximum SRU temperature is 1125 K.

the evolution of the cathode and anode overpotentials at the initial time and after 4500 h of operation at a constant system specific power of 0.29 W cm^{-2} . The trends are similar when comparing profiles at the reference operating point, but less pronounced, due to the constant current density. The distribution of the cathode and anode overpotentials, unlike that of the current density, are more even in counter-flow, which accounts for its better resistance against cathode chromium contamination, resulting in better durability (see Fig. 2, and Part I [26] for an analysis over a wider range of operating conditions).

The overpotentials exhibit a small variation along the x direction and the pattern of their distribution does not drastically change because of degradation (Fig. 8). The anode diffusion overpotential in the counter-flow is an exception, which is explained by the highest molar fraction gradient through the anode in R_3 along the symmetry axis, at the fuel inlet (location A in Fig. 1). The trends

identified with the one-dimensional model are valid for the FlameSOFC SRU design. The counter-flow configuration, combined to a methane conversion fraction of 25% in the reformer provides the highest lifetime over the investigated range of operating conditions, despite the concentration of the current density. During operation, the increase of the current density should be compensated by a decrease of the fuel utilisation. As the present operating strategy does not include this refinement, the onset of diffusion limitation can occur in co-flow, in the zones of lean fuel mixtures and cause the reoxidation of the anode at the interface with the electrolyte [26].

4.4. Decrease of available triple-phase boundary in the electrodes

The evolution of the available TPB in the active area at the interface between the cathode and the electrolyte depicted along

the symmetry axis in Fig. 9 matches that of the overpotential (Fig. 8). Chromium contamination is accordingly more severe in the co-flow configuration. It affects predominantly the air inlet of the active area, where more than 80% of the initial TPB at the cathode/electrolyte interface is blocked after 4500 h. The oxygen reduction reaction can still proceed at these locations, but is shifted away from the electrolyte, resulting at the end in an electrochemical inactive layer, where only ohmic losses occur [32]. Chromium contamination proceeds accordingly, since it follows the local overpotential through the thickness of the composite cathode.

The reduction of the available TPB in the anode follows another trend than that of the cathode. It is slower in co-flow configuration, owing to the combination of low temperature and high hydrogen molar fraction close to the location of high current density. In both flow configurations, the coarsening is less severe in the fuel inlet side of the active area, which shows a predominant effect of the gas

composition in the model. The plateau nickel particle diameter is reached over most of the active area after 3000 h. The further evolution of the degradation is therefore due to interactions with the other processes. This behaviour may not fully reproduce the reality. It is a model limitation, due to the incomplete understanding and lack of quantitative characterisation of these degradation phenomena. Model improvements may be needed, depending on the stack technology to be studied, as the knowledge and information becomes available.

Chromium contamination is a major contribution among the selected degradation phenomena investigated in this study (Section 4.1). Fig. 10 displays the effect of the operating conditions on the averaged deposition rate in the cathode. The pattern follows that of the SRU potential depicted in Fig. 2 and the dependence on the operating conditions matches the observation on the evolution of ASR of the cathode (Section 4.1). The severity of cathode chromium contamination can be assessed from the initial averaged chromium deposition rate, since the curves do not cross during operation at constant system specific power.

Fig. 11 depicts the distribution of the local vaporisation rate from the MIC and deposition rate averaged in the thickness in the LSM–YSZ cathode. The air flow is one-dimensional in the Flame-SOFC design and variation of the overpotential is small along the x-axis. Therefore, only the results along the y-axis in R_3 are depicted. The local vaporisation rate varies along the flow path according to the temperature. It decreases during operation at a constant specific system power because of the increase of the air velocity and, to a lower extent, to the decrease of the average temperature due to the increase of the air ratio. The vaporisation rate is at least one order of magnitude higher than the averaged deposition rate. The latter does therefore not strongly influence the partial pressure of $p_{\text{CrO}_2(\text{OH})_{2(g)}}$ in the cathode gas. It is lower and more uniform in the counter-flow configuration, owing to the lower and more even distribution of the overpotential. A higher system specific power induces a higher deposition rate. The effect of the redistribution of the current density, and hence of overpotential, is well seen in the counter-flow configuration. At the air outlet, the peak in current density decreases, as this is the zone of highest overpotential,

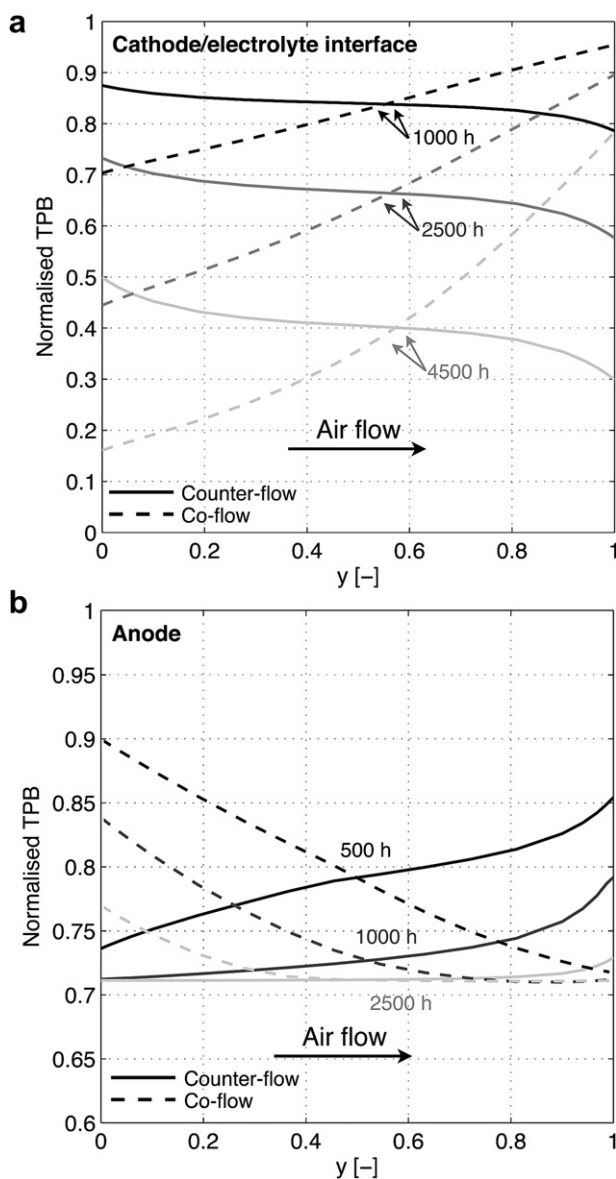


Fig. 9. Evolution of the relative TPB at (a) the cathode/electrolyte and (b) the anode/electrolyte interface in R_3 at the symmetry line during operation, at a constant system power of 0.29 W cm^{-2} in co- (dashed lines) and counter-flow configuration (solid lines).

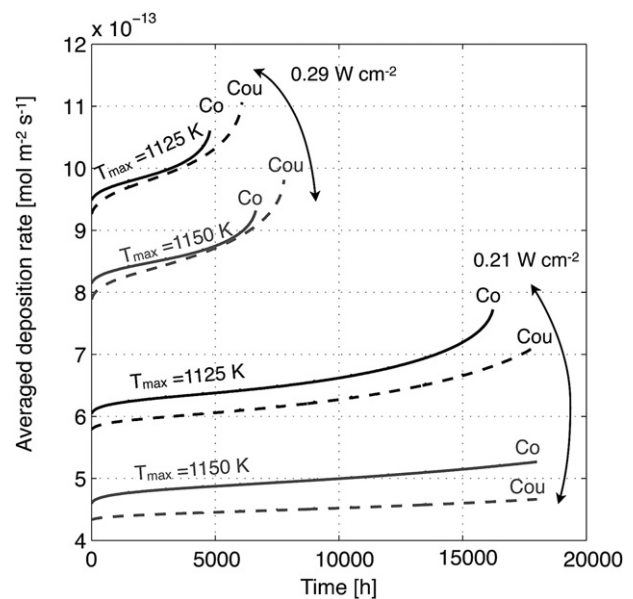


Fig. 10. (a) Evolution of the averaged deposition rate of $\text{CrO}_2(\text{OH})_2$ into Cr_2O_3 during operation at different constant specific system power, maximum allowable temperature, and flow configurations. The methane conversion fraction in the reformer is 0.25 (counter-flow, dashed lines) and 0.99 (co-flow, solid lines).

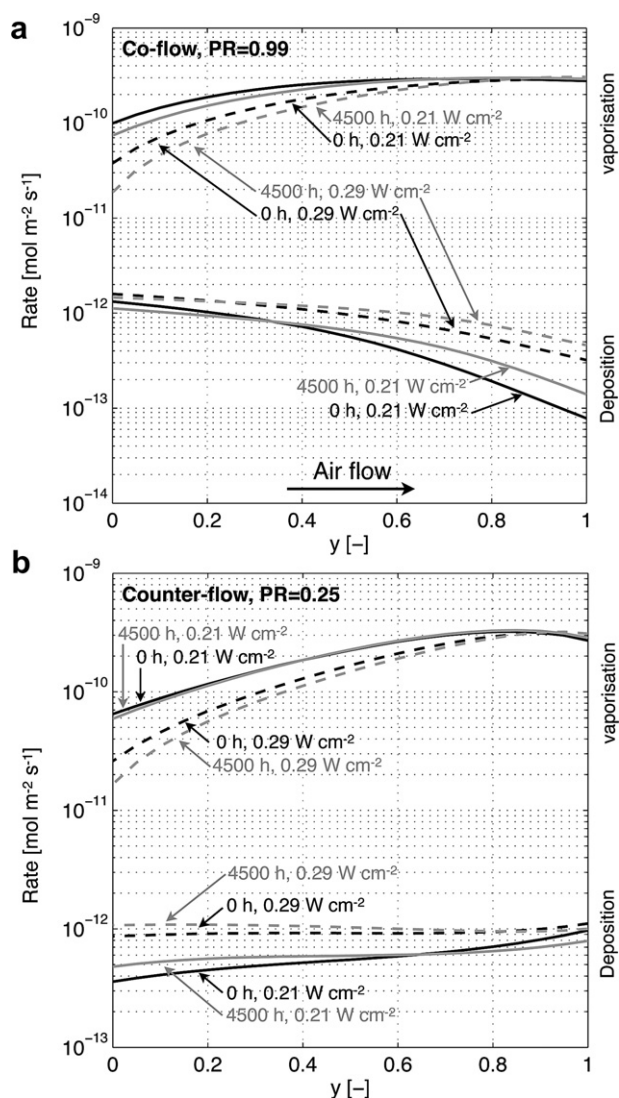


Fig. 11. Local chromium deposition and vaporisation rates along the symmetry axis of the active area R_3 at the initial time and after 5000 h of operation at a constant specific system power and a maximum allowable temperature of 1125 K. (a) Co-flow (b) counter-flow.

which yields a more even distribution of the overpotential and consequently of the averaged deposition rate.

Recently, owing to an accurate method developed for chromium detection, Schuler et al. [55] could demonstrate good correlation between cathode degradation and deposited chromium. It must be emphasised, however, that the correlation between cathode degradation and amount of chromium measured in post-test analysis is not necessarily simple. The possible deposition of chromium in the current collecting layers [47,56] and inactive zones of the functional electrode [46] affect the accuracy of the measurements. Because of the various materials used in the different layers of a state-of-the-art MEA, the deposit is unlikely a pure chromium oxide and may not completely prevent the oxygen reduction reaction. It can also promote morphological alteration of the electrode, which may also contribute to the degradation [56].

The location of the zone where LZO/SZO phases can first develop and decrease the available TPB, cannot be deduced strictly from the observation of the distribution of the cathode local overpotential. This process depends on temperature and oxygen partial pressure in the cathode, hence current density. Fig. 12 provides a schematic

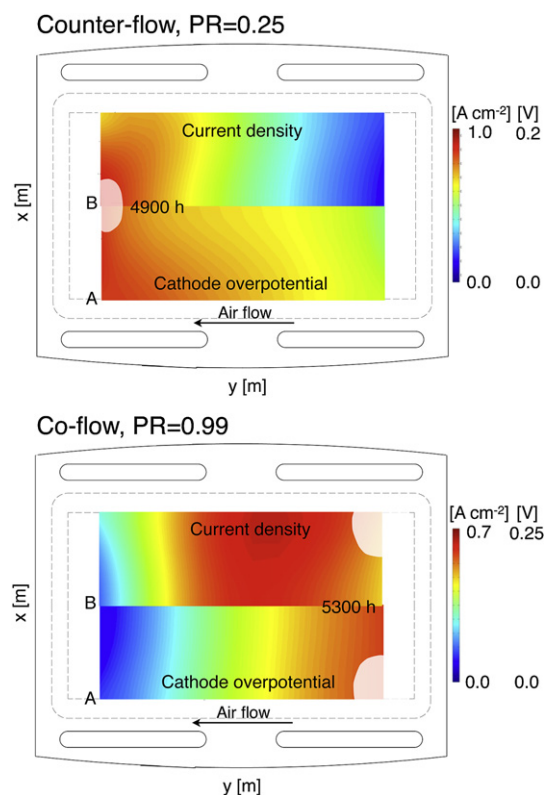


Fig. 12. Zones affected (coloured in beige) by the formation of LZO/SZO in the LSM-YSZ cathode, during operation at a constant SRU power of 0.32 W cm^{-2} . Maximum SRU temperature of 1125 K.

view of the critical zones, along with the distribution of the overpotential and current density. In the co-flow configuration, the effect of the overpotential dominates that of the temperature. Despite a marginally higher overpotential at location B than A, the formation first occurs close to the gasket/GDL frontier, because of the opposite profile along the x axis, of both current density and temperature. The operation times needed to activate the formation of LZO/SZO in constant SRU power output mode, predicted by the one- and two-dimensional models are comparable for the co-flow configuration (5500 h and 5300 h, see Part I [26]). In contrast, in the counter-flow configuration, the high current density at location B, promoted by the lateral fuel manifold and by low methane conversion in the reformer, is detrimental and significantly reduces the time to activate the formation of LZO/SZO. It is of 4900 h in the two-dimensional model instead of 5600 h in the one-dimensional model, whereas similar values of 4850 h and 4650 h are predicted by both models for a complete methane conversion in the reformer.

5. Conclusion

This investigation of the distribution and evolution of the degradation in a SOFC stack under practical operating conditions has highlighted detrimental interactions between the degradation processes at the SRU scale. IV characterisations performed at fixed operating times underestimate the severity of the degradation, compared with the fixed reference point procedure, due to temperature effects. The degradation processes affect the magnitude, rather than the patterns in the distribution of the polarisation losses. The contribution of the cathode, affected by chromium contamination that is driven predominantly by the overpotential, dominates.

The co-flow configuration is more sensitive to detrimental interactions between the degradation processes than counter-flow, because of the trade-off between high temperature and lean fuel mixture that governs the location of the zone of highest current density. This causes an increase of the diffusion and hydrogen oxidation losses in the anode and ohmic losses in the electrolyte, even after the variables that simulate their degradation in the model reach their plateau values. This is not observed in counter-flow, which furthermore yields a lower and more even distribution of the cathode overpotential, unlike that of the current density. Cathode chromium contamination is therefore alleviated and life-time extended.

In the conditions studied here, operation at low system specific power and high maximum allowable SRU solids temperature alleviates the degradation. Manufacturing limitations, costs and mechanical considerations must be further implemented in the analysis as they may balance the advantages provided by such a mitigation approach. Disparities in the anode GDL mechanical properties within the typical range for a metallic foam can alone cause the fuel starvation of an SRU in a stack and consequently reduce the lifetime. The benefit of lowering the cathode overpotential by increasing the operating temperature exceeds the detrimental higher release rate by the MIC of volatile chromium cathode-contaminating species and higher degradation of the 8YSZ ionic-conducting phases.

A complete (partial) methane conversion fraction in the upstream reformer is beneficial in co-flow (counter-flow), in accordance with the results presented in Part I. Combining internal reforming and counter-flow operation allows the highest lifetime for the Flame-SOFC SRU design as well, though the lateral fuel supply partially hinders the benefit. This design increases the maximum local current density. Because the cathode overpotential is in comparison less affected, the lifetime reduction is limited. The most significant effect is an earlier start of formation of zirconate in the LSM–YSZ cathode, compared with an ideal one-dimensional geometry.

Acknowledgements

This work was funded by the Swiss SOFC Consortium, co-financed by the Swiss Federal Office of Energy (SFOE) and Swiss-electric Research, contract number 152210, and the FP6 FLAME-SOFC European project, contract number CE-Flame SOFC-019875. gPROMS, a modelling tool from Process System Enterprise (PSE) has been used under academic licensing. Computations have been performed on the Pleiades2 cluster located at EPFL.

Appendix

Two-dimensional SRU model

The model is dynamic only in terms of degradation phenomena, because under constant system electrical power output, the temperature profile does neither evolve drastically nor within short time periods:

$$\lambda_s \nabla^2 T_s + \dot{Q}_{s_{rx}} + \dot{Q}_{s_{conv}} = 0 \quad (\text{A-1})$$

Heat transfer by convection between the gases and the solid structure and the thermal energy released by the chemical and electrochemical reactions are embedded in the rates of volumetric thermal energy generated, $\dot{Q}_{s_{conv}}$ and $\dot{Q}_{s_{rx}}$, respectively.

$$\dot{Q}_{s_{conv}} = \frac{h_g^c}{h_s} (T_g - T_s) \text{ in } \mathcal{R}_1, \mathcal{R}_5 \quad (\text{A-2})$$

$$\dot{Q}_{s_{conv}} = \sum_g \frac{h_g^c}{h_s} (T_g - T_s) \text{ in } \mathcal{R}_2, \mathcal{R}_3, \mathcal{R}_4 \quad (\text{A-3})$$

$$\dot{Q}_{s_{conv}} = 0 \text{ in } \mathcal{R}_6 - \mathcal{R}_{10} \quad (\text{A-4})$$

$$\begin{aligned} \dot{Q}_{s_{rx}} = & \frac{N_{\text{CH}_4}|_{\text{GDL-an}}}{h_s} (-dH_{\text{O}_{\text{SMR}}} - dH_{\text{O}_{\text{WS}}}) + \frac{N_{\text{CO}}|_{\text{GDL-an}}}{h_s} (-dH_{\text{O}_{\text{WS}}}) \\ & + \frac{j_{\text{tot}}}{2Fh_s} (-dH_{\text{O}_{\text{elchem}}}) - \frac{V \cdot j_u}{h_s} \end{aligned} \quad (\text{A-5})$$

At boundaries Γ_1 and Γ_2 , heat is transferred from the stack to the environment, by thermal radiation followed by conduction through the insulation. The exchange with above/underneath and front/rear nodes is neglected [57], whereas view factors are considered [37]:

$$\begin{aligned} \lambda_s n_{\Gamma_s} \cdot \nabla T_s + \frac{1}{A_{s-\Gamma_s}} \frac{\epsilon_s (T_s^4 - T_{isl}^4)}{\frac{1 - \epsilon_s}{\epsilon_s A_{s-\Gamma_s}} + \frac{1}{A_{s-\Gamma_s} \mathcal{F}_{s-isl-\Gamma_s}} + \frac{1 - \epsilon_{isl}}{\epsilon_{isl} A_{isl-\Gamma_s}}} \\ = 0, \text{ on } \Gamma_1, \Gamma_2 \end{aligned} \quad (\text{A-6})$$

$$\mathcal{F}_{s-isl-\Gamma_s} = \frac{[(W_{1s} + W_{2s})^2 + 4]^{1/2} - [(W_{2s} - W_{1s})^2 + 4]^{1/2}}{2W_{1s}} \quad (\text{A-7})$$

where $W_{1s} = A_{s-\Gamma_s}/(A_{isl-\Gamma_s})$, $W_{2s} = (A_{isl-\Gamma_s})/A_{s-\Gamma_s}$. The energy conservation on the insulation yields the insulation temperature:

$$\epsilon_s (T_s^4 - T_{isl}^4) = \frac{\lambda_{isl}}{h_{isl}} (T_{isl} - T_{amb}) \text{ on } \Gamma_1, \Gamma_2 \quad (\text{A-8})$$

Despite the simplifications, Ref. [15] has shown that such an approach can reasonably capture the temperature distribution in a segmented-cell SRU.

The conservation of energy of gases as well as the conservation of species accounts for variations in gas densities:

$$\rho_g \mathbf{u}_g \cdot \nabla H_g + H_g \sum \mathfrak{R}_k^m = \dot{Q}_{g_{rx}} + \dot{Q}_{g_{conv}} \text{ in } \mathcal{R}_1 - \mathcal{R}_5 \quad (\text{A-9})$$

$$\rho_g \mathbf{u}_g \cdot \nabla \omega_j + \omega_j \sum \mathfrak{R}_j^m = \frac{M_i N_i|_{\text{GDL-an}}}{h_g} \text{ in } \mathcal{R}_1 - \mathcal{R}_5 \quad (\text{A-10})$$

Ideal gas properties are assumed and computed from Todd et al. [58]. $\dot{Q}_{g_{conv}}$ and $\dot{Q}_{g_{rx}}$ are computed in a similar manner to $\dot{Q}_{s_{conv}}$ and $\dot{Q}_{s_{rx}}$, i.e. the energy released by the chemical reactions is computed from the balance of species at the anode–gas interface. The gas velocity is described by the common Darcy law, which is solved along with the mass conservation:

$$\mathbf{u}_g = \frac{B_o}{\mu_g} \nabla p \quad (\text{A-11})$$

$$\nabla \cdot (\rho_g \mathbf{u}_g) = \sum \mathfrak{R}_i^m \quad (\text{A-12})$$

Creep in gas-diffusion layers

Slight differences in relative density, combined to the limited number of struts in the thickness of a foam can significantly alter the creep strain rate at high temperature. Data on the creep

behaviour of dense nickel is corrected by a scaling equation for cellular solids [53,54]:

$$\dot{\epsilon} = k_0 \exp\left(-\frac{E_a}{RT}\right) \left(\frac{1}{3} \frac{\rho^*}{\rho}\right)^{-m} \sigma^m \quad (\text{A-13})$$

For a first investigation, the assembly load is assumed to provoke a uniform deformation. The foam relative density is 7.5%. The temperature (1073 K) and compression stress (0.15 MPa [12]) are uniform. The irreversible creep strain at any time is:

$$\dot{\epsilon} = k_0 \sigma^m \quad (\text{A-14})$$

Here, $k_0 = 1.44 \cdot 10^{-3} \text{ (MPa}^{-m} \text{ h}^{-1})$ and $m = 4.6$. This relation gives an irreversible strain of 0.23%, after 10000 h of operation. The correction of the anode gas flux proceeds by comparing the nominal situation with a worst case, respectively characterised by the aforementioned creep strain rate (Eq. A-14) and one twice higher. Notwithstanding the effects of the struts, such variation corresponds to a decrease of 1% in relative density of the metallic foam. The gas flow is adapted for the change in permeability (Part I [26]) and reduced section. For a comprehensive analysis, the overall bending of an SRU in a stack and the creep behaviour of components adjacent to the GDL, as well as thermal coupling between SRUs unevenly supplied in fuel, should be accounted for.

Nomenclature

Latin letters

A	area (m^2)
A_{TPB}	specific area at the triple phase boundary ($\text{m}^2 \text{ m}^{-3}$)
B_o	permeability in porous medium (m^2)
D_{ij}^e	effective bulk diffusivity of binary pair in porous medium ($\text{m}^2 \text{ s}^{-1}$)
E_a	activation energy (J mol^{-1})
F	Faraday's constant 96485 (C mol^{-1})
H	gas enthalpy (J kg^{-1})
h	thickness (m)
h^c	convection heat transfer coefficient ($\text{W m}^{-2} \text{ K}^{-1}$)
i_o	exchange current density (A m^{-2})
j	current density (A m^{-2})
k_0	kinetic constant
L	length (m)
m^{CP}	creep stress exponent
M_i	molecular weight of species i (kg mol^{-1})
N_i	molar flux of species i ($\text{mol m}^{-2} \text{ s}^{-1}$)
Nu	Nusselt number
p	pressure (Pa)
p^{atm}	atmospheric pressure 101325 (Pa)
R	universal gas constant 8.314 ($\text{J mol}^{-1} \text{ K}^{-1}$)
T	temperature (K)
T_{amb}	ambient temperature, 298 (K)
u	gas velocity (m s^{-1})
V	potential (V)
W	ratio of areas
x_i	mole fraction of species i
\dot{Q}	volumetric rate generated thermal energy (W m^{-3})
\mathcal{F}	view factor, dimensionless
\mathcal{V}	volume (m^3)
\mathcal{R}_i	rate of production of species i ($\text{mol m}^{-3} \text{ s}^{-1}$)
\mathcal{R}_i^m	rate of production of species i due to electrochemical reaction ($\text{kg m}^{-3} \text{ s}^{-1}$)

Greek letters

ϵ	strain
η	overpotential (V)

λ	thermal conductivity ($\text{W m}^{-1} \text{ K}^{-1}$)
μ_g	viscosity (Pa s)
ω	mass fraction of species i , dimensionless
ρ	density (kg m^{-3})
ρ^*	foam density (kg m^{-3})
σ	stress (Pa)
ϵ	emissivity
ς	Stefan–Boltzmann constant ($5.670 \cdot 10^{-8} \text{ (W m}^{-2} \text{ K}^{-4})$)

Indices

elchem	electrochemical
an	anode
cath	cathode
conv	convection
g	index for gases, either air or fuel
isl	insulation
j	index for gas species
rx	reaction
s	index for solid parts, individual components or averaged structure
tot	total
u	useful
\mathcal{D}	degradation

Superscripts

dep	deposition
eq	equilibrium
vap	vaporation

Acronyms

ASR	area specific resistance
GDL _i	gas-diffusion layer, a: anode, c: cathode
IV	current-voltage
LSM	lanthanum strontium manganite
LZO	lanthanum zirconate
MIC	metallic interconnect
PR	methane conversion fraction in the reformer
SRU	single repeating unit
SZO	strontium zirconate
TPB	triple phase boundary
YSZ	yttria-stabilised zirconia

References

- [1] M.A. Khaleel, Z. Lin, P. Singh, W. Surdoyal, D. Collin, Journal of Power Sources 130 (2004) 136–148.
- [2] V.M. Janardhanan, V. Heuveline, O. Deutschmann, Journal of Power Sources 172 (2007) 296–307.
- [3] T.X. Ho, P. Kosinski, A.C. Hoffmann, A. Vik, Chemical Engineering Science 64 (2009) 3000–3009.
- [4] T.X. Ho, P. Kosinski, A.C. Hoffmann, A. Vik, Chemical Engineering Science 63 (2008) 5356–5365.
- [5] C. Stiller, B. Thorud, O. Bolland, R. Kandepu, L. Imsland, Journal of Power Sources 158 (2006) 303–315.
- [6] F. Mueller, F. Jabbari, R. Gaynor, J. Brouwer, Journal of Power Sources 172 (2007) 308–323.
- [7] P. Aguiar, C. Adjiman, N. Brandon, Journal of Power Sources 138 (2004) 120–136.
- [8] P. Aguiar, C. Adjiman, N. Brandon, Journal of Power Sources 147 (2005) 136–147.
- [9] A. Selimovic, M. Kemm, T. Torisson, M. Assadi, Journal of Power Sources 145 (2005) 463–469.
- [10] C.-K. Lin, T.-T. Chen, Y.-P. Chyou, L.-K. Chiang, Journal of Power Sources 164 (2007) 238–251.
- [11] A. Nakajo, C. Stiller, G. Härkegård, O. Bolland, Journal of Power Sources 158 (2006) 287–294.
- [12] A. Nakajo, Z. Wuillemin, J. Van herle, D. Favrat, Journal of Power Sources 193 (2009a) 203–215.
- [13] A. Nakajo, Z. Wuillemin, J. Van herle, D. Favrat, Journal of Power Sources 193 (2009b) 216–226.

- [14] Z. Wuillemin, N. Autissier, A. Nakajo, M.-T. Luong, J. Van herle, D. Favrat, *Journal of Fuel Cell Science and Technology* 5 (2008) 011016–011019.
- [15] Z. Wuillemin, *Experimental and Modeling Investigations on Local Performance and Local Degradation in Solid Oxide Fuel Cells*, Ph.D. thesis, 4525, Lausanne, 2009.
- [16] J. Gazzarri, O. Kesler, *Journal of Power Sources* 176 (2008) 138–154.
- [17] D. Larrain, J. Van herle, D. Favrat, *Journal of Power Sources* 161 (2006) 392–403.
- [18] S. Koch, P. Hendriksen, M. Mogensen, Y. Liu, N. Dekker, B. Rietveld, B. de Haart, F. Tietz, *Fuel Cells-From Fundamentals to Systems* 6 (2006) 130–136.
- [19] A. Hagen, R. Barfod, P. Hendriksen, Y. Liu, S. Ramousse, *Journal of the Electrochemical Society* 153 (2006) A1165–A1171.
- [20] A. Hagen, Y.L. Liu, R. Barfod, P.V. Hendriksen, *Journal of the Electrochemical Society* 155 (2008) B1047–B1052.
- [21] Y. Liu, A. Hagen, R. Barfod, M. Chen, H. Wang, F. Poulsen, P. Hendriksen, *Solid State Ionics* 180 (2009) 1298–1304.
- [22] L. de Haart, J. Mougin, O. Posdziech, J. Kiviahio, N. Menzler, *Fuel Cells* 9 (2009) 794–804.
- [23] N.H. Menzler, L.G. de Haart, D. Sebold, *ECS Transactions* 7 (2007) 245–254.
- [24] L. Holzer, B. Iwanschitz, T. Hocker, B. Münch, M. Prestat, D. Wiedenmann, U. Vogt, P. Holtappels, J. Sfeir, A. Mai, T. Graule, *Journal of Power Sources* 196 (2011) 1279–1294.
- [25] M. Fardadi, F. Mueller, F. Jabbari, *Journal of Power Sources* 195 (2010) 4222–4233.
- [26] A. Nakajo, F. Mueller, J. Brouwer, J. Van herle, D. Favrat, *Progressive activation of degradation processes in solid oxide fuel cells stacks: Part I: Lifetime extension by optimisation of the operating conditions*, *Journal of Power Sources* 216 (2012) 449–463.
- [27] gPROMS (General Process Modelling and Simulation Tool), v3.2, Process Systems Enterprise Ltd., London.
- [28] A. Nakajo, Z. Wuillemin, P. Metzger, S. Diethelm, G. Schiller, J. Van herle, D. Favrat, *Journal of the Electrochemical Society* 158 (2011) B1083–B1101.
- [29] F.H. van Heuveln, H.J.M. Bouwmeester, *Journal of the Electrochemical Society* 144 (1997) 134–140.
- [30] E. Achenbach, E. Riensche, *Journal of Power Sources* 52 (1994) 283–288.
- [31] H. Zhu, R.J. Kee, V.M. Janardhanan, O. Deutschmann, D.G. Goodwin, *Journal of the Electrochemical Society* 152 (2005) A2427–A2440.
- [32] A. Nakajo, P. Tanasini, S. Diethelm, J. Van herle, D. Favrat, *Journal of the Electrochemical Society* 158 (2011) B1102–B1118.
- [33] W. Liu, X. Sun, E. Stephens, M. Khaleel, *Journal of Power Sources* 189 (2009) 1044–1050.
- [34] E. Opila, N. Jacobson, D. Myers, E. Copland, *JOM Journal of the Minerals, Metals and Materials Society* 58 (2006) 22–28.
- [35] B.B. Ebbinghaus, *Combustion and Flame* 93 (1993) 119–137.
- [36] B.B. Ebbinghaus, *Combustion and Flame* 101 (1995) 311–338.
- [37] F. Incropera, D. DeWitt, T. Bergman, A. Lavine (1996).
- [38] J. Froitzheim, G. Meier, L. Niewolak, P. Ennis, H. Hattendorf, L. Singheiser, W. Quadackers, *Journal of Power Sources* 178 (2008) 163–173.
- [39] G.R. Holcomb, D.E. Alman, *Scripta Materialia* 54 (2006) 1821–1825.
- [40] S.P. Jiang, J.P. Zhang, L. Apateanu, K. Foger, *Journal of the Electrochemical Society* 147 (2000a) 4013–4022.
- [41] S.P. Jiang, J.P. Zhang, K. Foger, *Journal of the Electrochemical Society* 147 (2000b) 3195–3205.
- [42] S.P. Jiang, J.P. Zhang, K. Foger, *Journal of the Electrochemical Society* 148 (2001) C447–C455.
- [43] J.W. Fergus, *International Journal of Hydrogen Energy* 32 (2007) 3664–3671.
- [44] J. Nielsen, A. Hagen, Y. Liu, *Solid State Ionics* 181 (2010) 517–524.
- [45] E. Konyseva, H. Penkalla, E. Wessel, J. Mertens, U. Seeling, L. Singheiser, K. Hilpert, *Journal of the Electrochemical Society* 153 (2006) A765–A773.
- [46] T. Horita, Y. Xiong, M. Yoshinaga, H. Kishimoto, K. Yamaji, M.E. Brito, H. Yokokawa, *Electrochemical and Solid-State Letters* 12 (2009) B146–B149.
- [47] A. Neumann, N.H. Menzler, I. Vinke, H. Lippert, *ECS Transactions* 25 (2009) 2889–2898.
- [48] N. Dukhan, *Experiments in Fluids* 41 (2006) 665–672.
- [49] D. Larrain, J. Van herle, F. Maréchal, D. Favrat, *Journal of Power Sources* 131 (2004) 304–312.
- [50] A. Nakajo, F. Mueller, J. Brouwer, J. Van herle, D. Favrat, *International Journal of Hydrogen Energy* 37 (2012a) 9249–9268.
- [51] A. Nakajo, F. Mueller, J. Brouwer, J. Van herle, D. Favrat, *International Journal of Hydrogen Energy* 37 (2012b) 9269–9286.
- [52] J. Van herle, D. Perednis, K. Nakamura, S. Diethelm, M. Zahid, A. Aslanides, T. Somekawa, Y. Baba, K. Horiuchi, Y. Matsuzaki, M. Yoshimoto, O. Bucheli, *Journal of Power Sources* 182 (2008) 389–399.
- [53] M. Ashby, H. Frost, *Deformation Mechanism Maps: The Plasticity and Creep of Metals and Ceramics*, Pergamon Press, 1982.
- [54] L. Gibson, M. Ashby, *Cellular Solids: Structure and Properties*, Cambridge University Press, 1999.
- [55] J.A. Schuler, P. Tanasini, A. Hessler-Wyser, J. Van herle, *Scripta Materialia* 63 (2010) 895–898.
- [56] N.H. Menzler, I. Vinke, H. Lippert, *ECS Transactions* 25 (2009) 2899–2908.
- [57] C. Stiller, B. Thorud, S. Seljebø, Ø. Mathisen, H. Karoliussen, O. Bolland, *Journal of Power Sources* 141 (2005) 227–240.
- [58] B. Todd, J.B. Young, *Journal of Power Sources* 110 (2002) 186–200.
- [59] ThyssenKrupp, *Material data sheet no. 4046*.